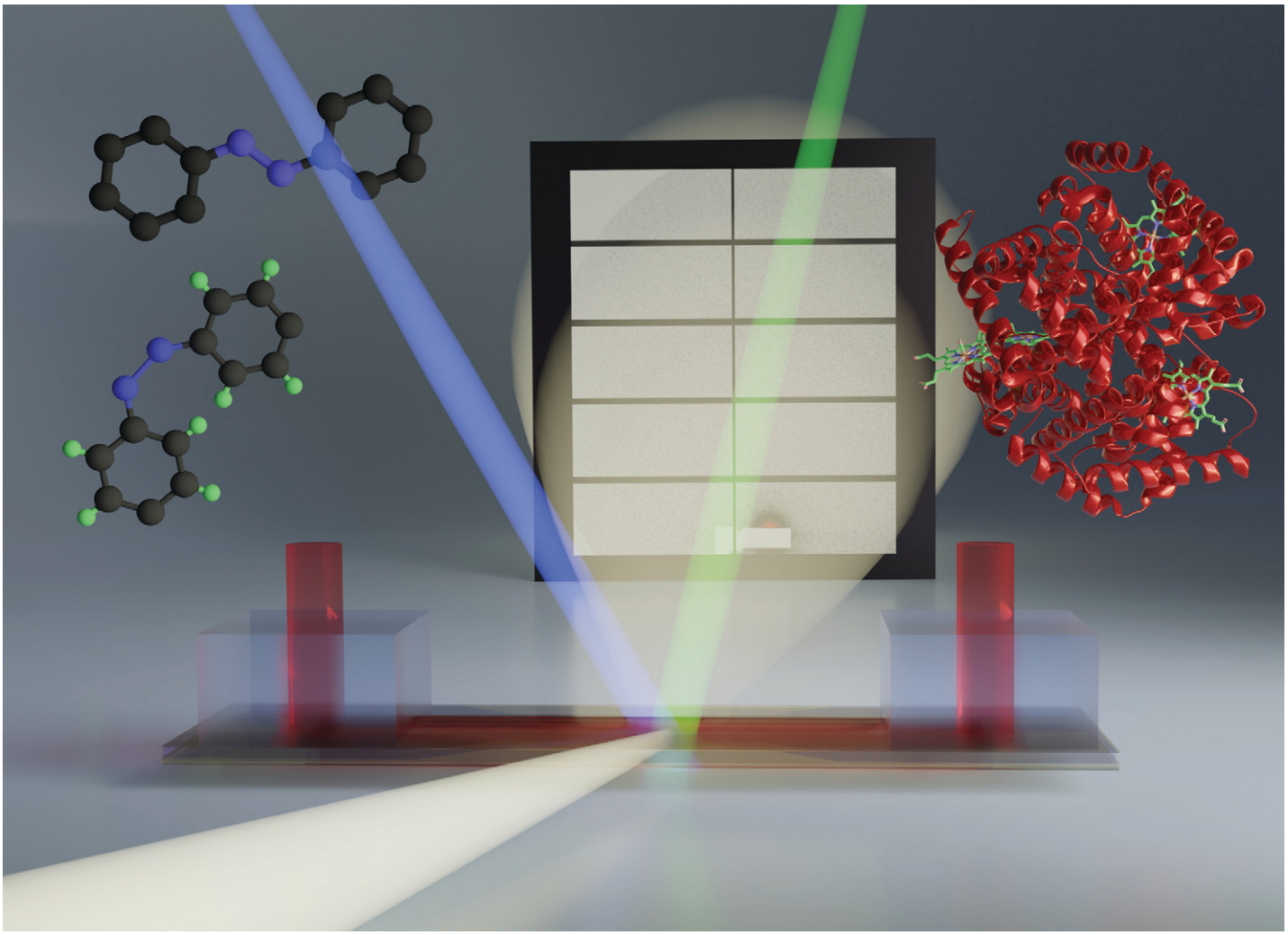

Showcasing research from Prof. Heinz Amenitsch, Institute of Inorganic Chemistry, Graz University of Technology, Austria.

Multi-wavelength transparent microfluidic device for UV-visible illumination and X-ray scattering studies of photoactive systems

This work presents a novel microfluidic device that is designed for simultaneous photoexcitation and X-ray scattering, which is fundamental for studying rapid structural transitions of photoactive materials. The device is transparent to UV-visible light in one direction and to X-rays in the perpendicular direction, and its capability has been demonstrated through successful experiments with hemoglobin and azobenzene derivatives.

Image reproduced by permission of Benedetta Marmiroli, Sumea Klokic from *Lab Chip*, 2026, **26**, 2697.

As featured in:

See Benedetta Marmiroli, Sumea Klokic *et al.*, *Lab Chip*, 2026, **26**, 2697.

ROYAL SOCIETY OF CHEMISTRY

rsc.li/loc

Registered charity number: 207890

Lab on a Chip

PAPER

View Article Online
View Journal | View Issue

Cite this: *Lab Chip*, 2026, **26**, 2697

Multi-wavelength transparent microfluidic device for UV-visible illumination and X-ray scattering studies of photoactive systems

Benedetta Marmiroli, *[a] Sumea Klokic, *[a] Barbara Sartori, [a] Marie Reißenbüchel,[a] Alessio Turchet[b] and Heinz Amenitsch [a]

Microfluidic devices are increasingly used in synchrotron-based experiments to deliver and probe liquid samples, offering advantages such as minimal sample consumption and reduced radiation damage. Despite their growing use, few devices have been specifically designed for monitoring liquids under photoexcitation, a promising approach for fast structural transitions. Here, a microfluidic device is presented that is transparent to X-rays in one direction and simultaneously transmits UV and visible light illumination to the sample in the perpendicular direction. The device is fabricated using lamination and UV lithography on a dry-film resist, eliminating the need for cleanroom facilities and simplifying production. Its multi-wavelength transparency was validated through UV-vis spectroscopy, where photoexcitation at different wavelengths induced reversible *trans*-to-*cis* isomerization of azobenzene and fluoro-azobenzene. X-ray transparency was verified through small-angle X-ray scattering (SAXS) measurements on hemoglobin and CO-ligated hemoglobin, both of which are sensitive to quaternary structural changes. These results confirm the suitability of the device for resolving protein structures and detecting subtle conformational changes of the type commonly encountered in photo-induced modulation. Initial proof-of-concept measurements demonstrate the feasibility of temperature-jump (T-jump) experiments, and the same architecture is readily extendable to time resolved pump–probe studies, providing a versatile platform for studying structural evolution in liquid samples using synchrotron SAXS.

Received 3rd December 2025,
Accepted 23rd March 2026

DOI: 10.1039/d5lc01116g

rsc.li/loc

Introduction

Light-responsive materials have emerged as a central focus in diverse areas of the natural sciences. Upon illumination, photoactive molecules and supramolecular assemblies can undergo reversible structural changes altering properties such as geometry, polarity, or flexibility.[1] Light is a particularly attractive stimulus for controlling biological functions, as its intensity and wavelength can be precisely regulated, enabling non-invasive, localized activation with micrometre-scale spatial resolution.[2] A well-known example is the photoactive molecule retinal, which enables vision in mammals through a light-induced conformational change. This has inspired the development of artificial systems such as photoreversible DNA and protein binding.[3,4] Moreover, incorporating photoactive groups into biomolecules has become an effective strategy to modulate biological activity, as demonstrated by photoactivated drugs that exhibit light-controlled enzyme activity,[1,5] receptor affinity,[6] or targeted antibiotic action.[1] Among these photoactive groups, those that undergo photoisomerization such as azo-groups, commonly referred to as photoswitches, are among the most extensively studied.[7–10] Because light can be delivered with high spatial and temporal precision, it provides an ideal trigger for inducing controlled structural changes and the associated dynamic responses. Investigating the dynamics during photoexcitation of proteins such as rhodopsin[11] and CO-ligated hemoglobin (HbCO),[12] or of lipids specially tailored for optopharmacology (the use of light to control drug activity),[10] is crucial for understanding the timescales of light-induced processes.[13] Several structural investigations have already been conducted using techniques based on X-rays, generated by high brilliance synchrotron radiation sources, particularly X-ray diffraction, wide angle X-ray scattering (WAXS), and small angle X-ray scattering (SAXS).[8,14–19] Among these, synchrotron SAXS is widely used in structural biology for nanostructural characterization typically in the 1–100 nm range. These techniques are particularly suitable for time-resolved measurements, as demonstrated by Cammarata *et al.*[12] Here, time-resolved WAXS was used to reveal coordinated molecular motions during carbon monoxide (CO) binding and photodissociation in hemoglobin (Hb).[12] Such insights are essential for understanding the transition pathway from

[a] *Institute of Inorganic Chemistry, Graz University of Technology, Graz, Austria. E-mail: benedetta.marmiroli@tugraz.at, sumea.klokic@tugraz.at*
[b] *Elettra-Sincrotrone Trieste, Basovizza, Trieste, Italy*

excitation to subsequent structural dynamics, and highlight the increasing use of photosensitive proteins as model systems to investigate inter- and intramolecular motions that are fundamental to biological and medical processes.[20]

However, such investigations remain challenging mainly due to the constraints imposed on suitable sample holders. In strongly absorbing samples, light penetration is limited, and consequently the illuminated volume must be comparable to or smaller than the optical attenuation length.[21] Microfluidic channels address this issue effectively, as their geometry can be precisely tailored to achieve sample depths on the order of the optical penetration length, ensuring uniform excitation of the entire sample volume. For protein samples in particular, microfluidic devices have become increasingly popular,[22,23] offering several key advantages: low sample consumption (critical for scarce protein systems), precise control of diffusion within microchannels (enabling rapid and accurate mixing), and efficient heat transfer due to their high surface-to-volume ratio, making them ideal for studying sensitive biological processes. Furthermore, microfluidic devices enhance the efficiency of solution-based synchrotron X-ray experiments, particularly SAXS, offering a versatile platform for investigating light-responsive samples while simultaneously enabling precise manipulation and delivery of liquids.[24–26] Beyond these advantages, microfluidic devices connected to pumps continuously refresh the liquid sample in front of the X-ray beam, mitigating radiation damage effects provoked by its high intensity.

Although several microfluidic devices have been reported for light manipulation of samples,[27] only a limited number allows multi-wavelength transparency.[26,28] In a previously reported experiment, a square capillary (0.1 × 0.1 mm) connected to two reservoirs was used for manipulating starch granules with optical tweezers, while simultaneously measuring their structure with SAXS.[29,30] However, the size of the device is not scalable and is therefore restricted to microfocus beamlines, where the dimension of the X-ray beam is smaller than the dimension of the channel, to avoid refraction effects due to the channel walls. A similar approach was used to combine optical tweezers with X-ray fluorescence.[31] A customized observation cell[32] and a Y shaped mixer connected to a quartz capillary[33] were employed for SAXS and UV-vis studies of nanoparticles nucleation and growth. More recently, simultaneous UV-visible and X-ray absorption spectroscopy measurements were conducted on a Kenics mixer with a quartz capillary.[34] Furthermore, a sample mixer based on careful material selection for UV and X-ray transparency was reported that allows spatially separated, yet continuous SAXS and UV-vis monitoring.[35]

In the particular case of photoexcitation experiments, microfluidic devices overcome some limitations encountered in standard capillaries, as they enable independent optimization with respect to the illumination geometry, to X-ray photon energy and brilliance, and to the sample type. In fact, light penetration, essential for maximizing the systems' photoresponse, depends on both the wavelength and the optical properties of the sample. Additionally, the sample concentration influences the intensity and possibility to resolve the X-ray scattering signal. This is also related to the brilliance and photon energy of the X-ray beam. Standard capillaries and other conventional sample holders are typically compatible only with specific X-ray sources or illumination set-ups. In this research, both the selection of materials and the development of a tailored fabrication protocol for a microfluidic device specifically engineered for combined photoexcitation and X-ray experiments are presented. A schematic of the device with its constituent materials is shown in Fig. 1(a), while the measurement concept to test the device is depicted in Fig. 2(a). To achieve both X-ray transparency along the beam path and illumination with UV and visible light in the perpendicular direction, SUEX dry film and impact modified poly(methyl

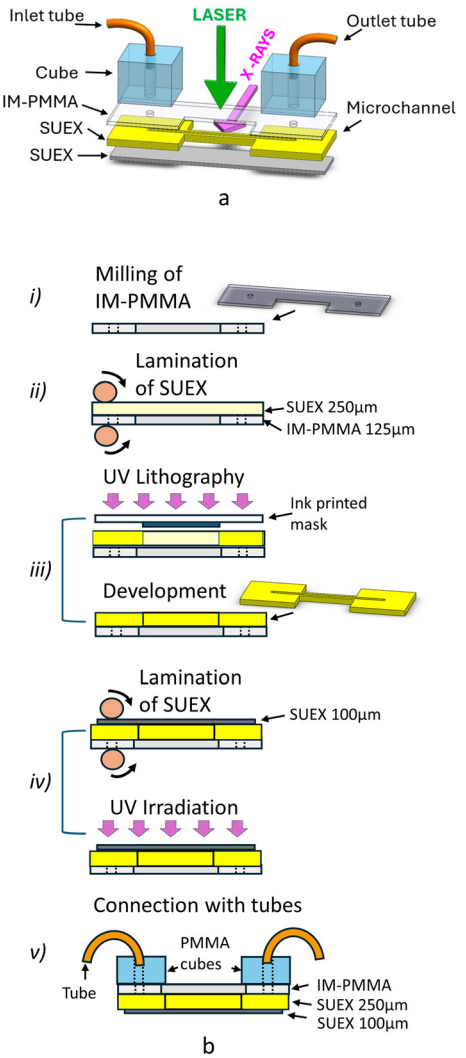

Fig. 1 (a) Exploded scheme of the microfluidic device showing the direction of the laser light and of the X-rays. The employed materials are indicated. (b) Scheme of the fabrication process of the proposed microchannel. i) Milling of the IM-PMMA slide in the desired shape, and drilling of holes. ii) Lamination of a 250 µm SUEX film on IM-PMMA. iii) UV lithography through a mask and developing process of the 250 µm SUEX film. iv) Lamination of a 100 µm SUEX film and subsequent irradiation with UV. v) Connection of the microchannel to external tubes.

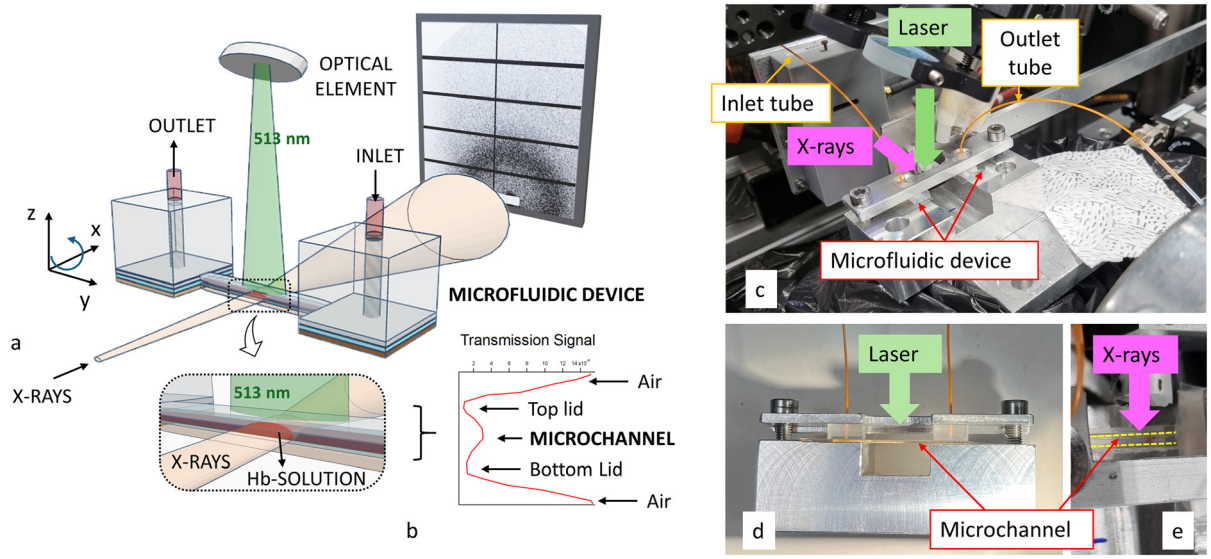

Fig. 2 (a) Scheme of the experimental set-up showing the microchannel, the detector, the X-ray beam path and the 513 nm laser light path. The direction of X-rays and of the sample movements are also shown, where *x* is the direction of X-rays, *z* is the direction of the laser perpendicular to the microchannel, *y* is the direction along the channel. (b) Magnification of the investigated area, and transmission signal employed to align the position of the channel to the X-ray beam. (c) Experimental set-up of the device mounted in the sample holder at the Austrian SAXS beamline. The directions of the X-rays and laser beam are indicated by arrows, as is the rough position of the microchannel and of the tubes. (d) Side view of the sample holder where the microchannel is mounted. The direction of the laser illumination is shown. (e) Magnification of the top view of the microchannel in the sample. The yellow dashed lines are a guide for the eye indicating the walls of the microchannel. The direction of the X-rays is shown.

methacrylate) (IM-PMMA) were selected. The microchannel was fabricated by a sequence of lamination and optical lithography steps, with the detailed protocol outlined in this work. While SUEX has previously been employed for microfluidic circuits,[36,37] to our knowledge it has never been used in combination with X-ray techniques and in particular with SAXS. The ability to illuminate the sample at specific wavelengths in the UV and visible range was verified using UV-vis spectroscopy to detect the photoisomerization of azobenzene and fluoro-azobenzene. X-ray transparency was assessed using synchrotron SAXS measurements on Hb and HbCO protein solutions. The microfluidic channel depth was designed to remain below the UV attenuation length for photoactive proteins, based on photoexcitation studies in capillaries for HbCO. Collectively, these results demonstrate its proof of principle performance, confirming that the microfluidic device is suitable to study a broad range of photosensitive samples *via* independent synchrotron SAXS and visible spectroscopy experiments.

Experimental

Fabrication process

The selected geometry of the device consists of a single microchannel 1 mm wide, 40 mm long (15 mm in the X-ray accessible part) and 0.25 mm deep. The thickness of the device walls in the X-rays accessible part is 0.5 mm. The materials employed for the device and the shape of the channel are shown in the exploded scheme of Fig. 1(a), while an outline of the fabrication process of the microchannel can be found in Fig. 1(b).

The fabrication process is considered green as it is based on the dry film SUEX,[38] and it does not require a clean room facility. It can be described in the following steps:

i. Milling of a 125 μm IM-PMMA sheet (Goodfellow Cambridge Ltd, UK) and drilling of two 1 mm diameter holes in order to add the tubing for feeding the channel in a later stage (*vide infra*, step v). The shape of the IM-PMMA was chosen to ensure an unobstructed path for the scattered X-rays (Fig. 1(b) step i).

ii. Lamination of 250 μm thick SUEX photosensitive negative resist (micro resist technology GmbH, Germany) on IM-PMMA. The two slides were put on a thin aluminium plate between two 400 μm thick spacers and laminated at 60 °C for three times, in order to ensure the adhesion of the SUEX to IM-PMMA, using the rolling mill system Falcon K (BlackHole Lab, France) (Fig. 1(b) step ii).

iii. UV lithography. Exposure of the laminated SUEX on IM-PMMA to UV light through an optical mask made of an ink printed acetate transparent sheet. This rather simple mask was chosen as the dimensions of the channel and its features do not require high resolution. UV lithography was conducted using a Mask Aligner UV KUB-3 (Kloé, France) with a power density of 21 mW cm^{-2} for 32 s. The post exposure bake was performed in an oven (Carbolite Gero Ltd, UK) at 85 °C for 40 minutes. At the end of the heating treatment, the piece was left to cool to room temperature inside the oven. The SUEX was then developed in mr-DEV 600 solution (micro resist technology GmbH) for 60 min

(Fig. 1(b) step iii). The developing time was carefully tuned, as the mr-DEV 600 is partially dissolving IM-PMMA. The piece was then rinsed in isopropanol (Merck KGaA, Darmstadt, Germany) and dried with a nitrogen stream.

iv. Sealing of the channel. A 100 μm thick SUEX was laminated on top of the channel at 50 °C for two times using the same aluminium slide with spacers as before (see step ii). Then UV lithography was performed without mask with a power density of 21 mW cm^{-2} for 21 s in order to crosslink the resist (Fig. 1(b) step iv). Post exposure bake was made at 85 °C for 40 minutes in the oven where afterwards the device was left cooling.

v. Connection of the microfluidic device to the tubes for liquid transfer. First, two cubes made of PMMA containing a channel through their center were glued to IM-PMMA in correspondence of its holes (Fig. 1(b) step v). Subsequently, tubes of 800 μm external diameter were inserted into the cubes and glued using standard acrylic glue.

An adequate stainless steel sample holder was fabricated to hold the microfluidic circuit both in front of the X-rays and the laser. An image of the mask, of a 250 μm SUEX channel, and of the final device after step iv is shown in Fig. S1 of SI. A picture of the microfluidic device mounted in the sample holder at the experimental station is shown in Fig. 2(c), a side view in Fig. 2(d), and a magnification of the top view in Fig. 2(e).

Test of the microfluidic device

UV-vis measurements with light irradiation. First, the transparency of the device materials and of the microchannel within the UV-vis range was evaluated by UV-vis spectroscopy (Agilent Cary 60, Agilent, US). The resulting spectra are shown in Fig. S2 of SI. After the material selection, the ability of the device to transmit UV and visible light to the sample was validated by monitoring the photoisomerization of two photoswitches using UV-vis spectroscopy. The first photoswitch is azobenzene (AZB), which undergoes a reversible isomerization from *trans*-to-*cis* upon UV light (365 nm) irradiation, and from *cis*-to-*trans* when exposed to blue light (450 nm). The second, 2,2′,3,3′,5,5′,6,6′-octafluoroazobenzene (F8-AZB), allows the reversible photoinduced *trans*-to-*cis* isomerization upon irradiation with green light (532 nm), and the *cis*-to-*trans* with exposure to blue light (450 nm). AZB was purchased from TKI Chemicals, whilst F8-AZB was synthesized following the protocol reported in the paper of Rödl *et al.*[39] The microdevice was mounted on a transmission sample holder and inserted in the UV-vis spectrophotometer. Subsequently, the photoexcitation experiments were conducted, where ethanolic AZB or F8-AZB solutions were filled into the microfluidic channel and irradiated by light. The solutions containing the photoswitch were prepared by dissolving 10 mg each of AZB or F8-AZB in 1 ml of ethanol and diluting to 0.05 mM. The irradiation of the AZB solution was accomplished with a 365 nm (UV) LED diode (EOLD-365, OSA OPTOLIGHT GmbH, Germany) of 6 mW power for 1 min (*trans*-to-*cis*), and a 450 nm (blue) LED (PL450B, OSRAM Opto Semiconductors GmbH, Germany) with a power density of 80 mW for 1 min (*cis*-to-*trans*). The F8-AZB solution was irradiated using a 532 nm (green) diode (LDS5, Thorlabs, US) of 1 mW power for 3 min (*trans*-to-*cis*) and again the blue diode (450 nm) for 1 min (*cis*-to-*trans*). The photo-excitation of the respective solutions was performed by illuminating through the IM-PMMA side of the microfluidic device. A UV-vis spectrum was acquired after every illumination step, performing triplicate measurements for every solution. As comparison, the same experiment was conducted with AZB and F8-AZB solutions in a standard quartz cuvette (QS Hellma Analytics) of 1.5 mm × 1.5 mm light path. All the reported power values for the illumination sources are at the sample plane. Due to the divergence of the sources (≥15° nominally), the spot size near the sample was between 1 and 2 mm. The curves of the same experiment have been normalized to the maximum value of the highest absorbance spectrum, in order to better underline the changes, and to be able to compare the solution in the cuvette to the one in the microchannel. An approximate estimate of the *trans–cis* and *cis–trans* conversion percentage in the channel *versus* in a standard cuvette has been evaluated, based on eqn (S1) shown in paragraph 1 of SI.[40]

SAXS measurements

All X-ray scattering measurements were performed at the Austrian SAXS beamline[41] at Elettra synchrotron in Trieste (Italy). The sample-to-detector distance was set at 1250 mm providing a q-range $0.08 < q < 5.8$ nm^{-1}, where q denotes the magnitude of the scattering vector $q = 4\pi/\lambda \sin(\theta/2)$, with λ being the wavelength and θ the scattering angle. The beam size was 0.1 × 1.5 mm (vertical × horizontal). The angular scale of the detector was calibrated with silver behenate. The holder for the microfluidic channel was mounted on a motorized stage allowing to translate along the y and z direction in the plane perpendicular to the X-ray beam, and to rotate along the X-ray axis for precise alignment in transmission geometry (see Fig. 2(a)). For static measurements, the SAXS patterns were acquired for 10 s, while during photo-excitation experiments 1000 images of 0.1 s were acquired. The experimental parameters for different SAXS measurements are specified in the results and discussion paragraph.

A Pilatus3 1 M detector was used (Dectris Ltd, Baden, Switzerland) with active area 169 × 179 mm^2 and a pixel size of 172 μm, and the 2D detector images were azimuthally integrated using the data pipeline SAXSDOG, developed at the Austrian SAXS beamline for automatic data reduction.[42] Normalization, background subtraction and data processing of the resulting 1D data were conducted with IGOR pro (Wavemetrics, Inc., Lake Oswego, OR).

The low q-range part (0.38–0.47 nm^{-1}) of the scattering curves of the protein after buffer subtraction was considered to obtain the radius of gyration R_g,[43] which is related to the dimension of the protein, according to eqn (S2) reported in paragraph 2 of SI. The upper limit of the q-range for Guinier

approximation was selected following the guidelines for the publication of SAXS data of biomolecules in solution.[44] The pair distance distribution function $p(r)$, whose Fourier transformation averaged over all directions in space gives the scattering intensity $I(q)$, defined by eqn (S3) in SI,[43] was determined using the GNOM program from the ATSAS package 4.1.1.[45] The invariant Q, second moment of the scattering curve which is related to the electron density of the sample, was determined following eqn (S4), while the correlation length l_c, related to characteristic dimensions of the sample, was calculated using eqn (S5) as shown in the SI.[43]

Photoexcitation experiments performed in combination with SAXS measurements were accomplished using the optical on-line table available at the Austrian SAXS beamline.[46] A schematic of the experimental setup is shown in Fig. 2(a), emphasizing the 513 nm laser light transferred *via* motorized optical mirrors and lenses to overlap spatially with the X-ray beam. The microfluidic channel was positioned on the sample holder with its UV-transparent IM-PMMA side facing the incoming laser.[46] The light to initiate the photo-switch was delivered by the Yb:KGW femtosecond laser (PHAROS, Light Conversion, Lithuania), which allows to precisely control the power and thus the photoresponse of the sample. Photoexcitation experiments were conducted at three different laser powers by adjusting the laser transmission T at the sample plane: 2.6 mW (T = 5%), 62 mW (T = 50%), and 182 mW (T = 100%). The laser spot size was set to 3.5 mm FWHM.

SAXS measurements were conducted on human hemoglobin (Hb). To evaluate the scattering signal of the protein in the microchannel when compared to a standard capillary, a protein solution and the related buffer were measured for 10 s using either a quartz capillary of 1.5 mm of diameter, or the microfluidic device connected to a syringe pump (TSE System GmbH, Germany) to infuse the sample at a flow rate of 0.25 μl min^{-1}. As proof of principle of the performance of the microfluidic device under photoexcitation conditions, SAXS measurements were performed to study the structure of Hb stabilized by the presence of the ligand CO (HbCO) before and after green laser irradiation following previous literature protocols.[12]

Preparation of hemoglobin for SAXS measurements

25 mg of Hb (Merck KGaA, Germany) were dissolved in 1 ml of 50 mM Tris at pH 7.4. HbCO solution was prepared according to Cho *et al.*,[47] as follows: 25 mg of human Hb were dissolved in 10 ml of 50 mM Tris, pH 7.4. Subsequently, 10 μl of a solution of KCN 1 M were added to the Hb to obtain cyanomet hemoglobin (HbCN). Subsequently, 50 μl of 0.9 M $Na_2S_2O_4$ were added to the HbCN solution. The obtained $HbCNS_2$ solution was purged with CO gas for 30 minutes yielding HbCO.

Results and discussion

Characterization of the selected device materials

Measuring light-responsive samples, which requires both a light source and X-rays, demands a careful selection of materials for the microfluidic device, considering also the limitations due to the fabrication processes at the micro scale. In the configuration shown in Fig. 2(a), where the two light sources are arranged perpendicularly, the channel walls must be both resistant and transparent to X-rays, while providing a low background scattering signal. Moreover, the top lid must withstand and be transparent to wavelengths above 340 nm, while the bottom lid only needs to endure laser irradiation. To meet these requirements, SUEX and IM-PMMA were chosen as suitable materials to compose the device.

The transparency of the materials in the UV or visible range was evaluated by UV-vis spectroscopy, as shown in Fig. S2 of SI. For the top lid, the IM-PMMA slide of 125 μm thickness was chosen, as it is transparent both to visible light and to UV light down to a wavelength of 280 nm, while the bottom lid made of SUEX dry film photoresist is optically transparent. The transparency of the fabricated microchannel is also shown.

As far as the X-rays transparency and scattering are concerned, the device has been tailored for the Austrian SAXS beamline. The beamline operates at 8 keV (X-ray wavelength 0.154 nm) with a photon flux density at sample of 10^{12} ph s^{-1} mm^{-2} at 2 GeV. The X-ray transparency of SUEX was evaluated by considering its major component (mixture of epoxy resins) and calculating the attenuation length, which is the depth into the material along the surface normal for which the X-rays intensity decays to $1/e$ of its value at the surface. The procedure and the details are described in paragraph 3 of SI. In the present case, the attenuation length varies from 1.58 mm to 1.64 mm (the attenuation length of quartz at 8 KeV is 0.11 mm). Based on these values, it is possible to calculate the transmission of 0.154 nm X-rays through 0.5 mm of SUEX, which is approximately 73%. Therefore, the material is sufficiently transparent. To quantify the scattering signal of SUEX, its absolute scattering probability was calculated measuring the scattering curve of a 0.5 mm thick SUEX film and of a calibrated glassy carbon slide of 1.05 mm, following the method already reported by our group.[48] As the scattering probability of the glassy carbon, and the thickness of both glassy carbon and of SUEX are known, the absolute scattering probability can be derived from the measured scattering intensity curves. The result, presented in Fig. S3 of SI, shows that SUEX has an absolute scattering probability which is comparable to 1 mm of water at q values around 1 nm^{-1}, *i.e.* 0.0016 (the scattering intensity of water is 1.6328×10^{-2} cm^{-1} at 293 K).[49]

To ensure a reliable measurement of the scattering signal of the sample within the microfluidic device, the channel dimensions were chosen to achieve sufficient sample volume. The depth of 0.25 mm is larger than the vertical dimension of the scattering X-ray beam (0.1 mm) allowing to measure only the centre of the channel and to avoid refraction or parasitic scattering effects due to the top or the bottom channel lid. The length of the central part of the microfluidic device, accessible to X-rays, is 15 mm to allow scanning in the y direction (see Fig. 2(a)). This could be relevant for time-

resolved experiments under continuous flow, since every position corresponds to a different residence time of the sample inside the channel.

Photoexcitation performance of AZB derivatives

To demonstrate the feasibility of photoexciting a sample in the microchannel using light in the UV and visible regime, AZB and 8F-AZB were employed. Upon irradiation, both AZB and 8F-AZB undergo reversible *trans*-to-*cis* photoisomerization (Fig. 3(a) and (d)), resulting in distinct absorbance changes that can be monitored by UV-vis spectroscopy. For this purpose, ethanolic AZB or 8F-AZB were introduced into the microfluidic channel with a light path of 0.25 mm × 1 mm and illuminated with 365 nm/450 nm and 532 nm/450 nm light, respectively. The corresponding normalized UV-vis spectra before and after photoexcitation are presented in Fig. 3(b) and (e). To allow direct comparison with a standard measurement configuration, identical experiments were conducted in a standard cuvette with a 1.5 mm × 1.5 mm light path which is comparable to the capillary diameter used during SAXS experiments (*vide infra*), and the corresponding spectra are presented in Fig. 3(c) and (f). For the photo-switching of AZB (Fig. 3(b) and (c)), the monitored n → π* absorption band around 420 nm is sensitive to the *cis*-isomer population, which allowed to evaluate the extent of photoisomerization. Irradiation by 365 nm promotes the conversion of AZB to its *cis* conformer (Fig. 3(a)),[7] as evidenced by an increased absorption intensity both for the sample contained in the cuvette and for the one in the microchannel. Notably, the increase in absorbance (ΔA) observed for AZB in the microchannel (ΔA = 0.07) is more than double than that observed in the cuvette (ΔA = 0.029) under identical UV irradiation conditions. Intriguingly, for 8F-AZB (Fig. 3(e) and (f)), irradiation at 532 nm increases the *cis*-isomer population (Fig. 3(d)), as evidenced by the rise in absorbance, whereas 450 nm light induces a shift and decrease in absorbance, consistent with *cis*-to-*trans* reisomerization.[39] In the non-irradiated state, both *trans* and *cis* conformers coexist as observed for 8F-AB in both the cuvette and the microfluidic device (*vide infra*). Upon 532 nm irradiation, the cuvette exhibited a larger absorbance (ΔA = 0.1) than the microchannel (ΔA = 0.05). Conversely, after irradiation with 450 nm, the microchannel showed a significantly greater absorbance decrease (ΔA = 0.36) compared to the cuvette (ΔA = 0.16), along with a larger band shift (9 nm compared to 4 nm). The photoconverted fraction related to the *cis*-conformer ($R_{\%cis}$) and to the *trans*-conformer ($R_{\%trans}$) in the microchannel *versus* in the cuvette were calculated[40] considering absorbances at λ = 430 nm for AZB and λ = 420 nm for 8F-AZB,[50] with the results reported in Table 1.

It must be noted that in the case of AZB, both the *cis* and *trans*-isomer absorb at 430 nm, yet the observed changes are dominated by the individual *cis* or *trans* AZB-conformer dependent on the excitation wavelength used. For AZB, the

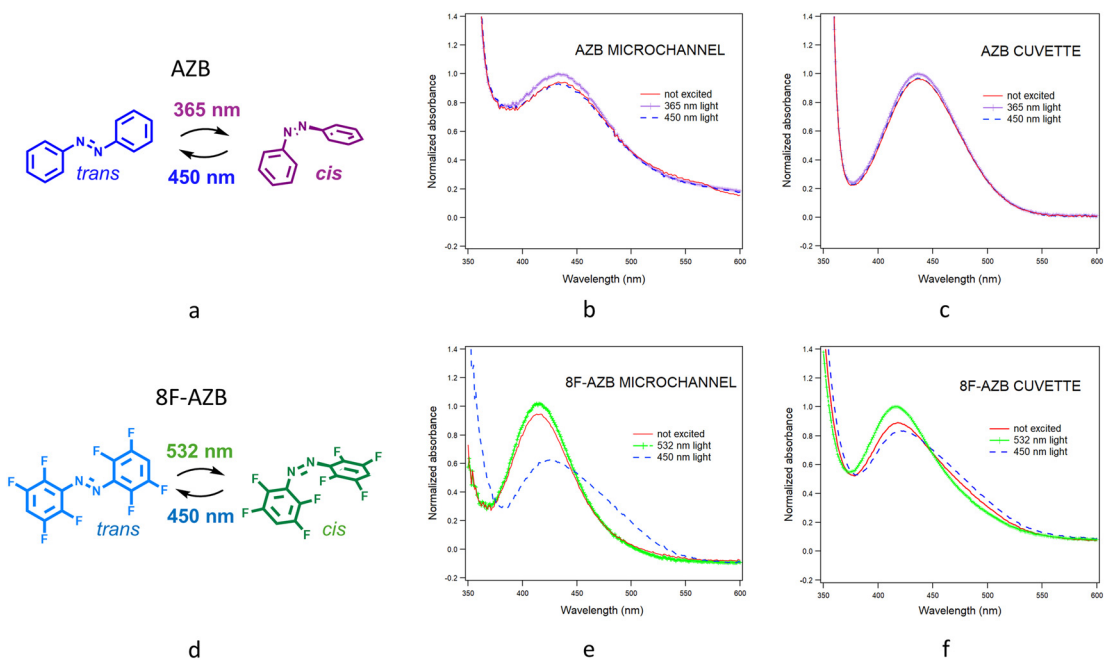

Fig. 3 (a) Scheme of the conformational changes of AZB after photoswitching. (b) UV-vis measurement of the photoswitching of AZB molecule in the microfluidic channel. Red curve is the initial AZB (not excited), violet curve with vertical bars is the AZB after 365 nm light irradiation, dashed blue curve corresponds to AZB after 450 nm light illumination to switch back. (c) UV-vis measurement of AZB switching in the cuvette. (d) Scheme of the conformational changes of 8F-AZB after photoswitching. (e) UV-vis measurement of the switching of the 8F-AZB molecule in the microfluidic channel. Red curve is the initial 8F-AZB (not excited), green curve with vertical bars is the 8F-AZB after 532 nm light irradiation, dashed blue curve corresponds to 8F-AZB after 450 nm light illumination. (f) UV-vis measurement of 8F-AZB switching in the cuvette.

Table 1 Photoexcited fraction of AZB and of 8F-AZB, both in the microchannel and in the cuvette upon light irradiation

	AZB		8F-AZB	
	Cuvette	Microchannel	Cuvette	Microchannel
$R_{\%cis}$	4.2%	6.9%	12%	6%
$R_{\%trans}$	3%	7.4%	16.5%	37%

converted fraction is rather low, yet the initial state as well as after 450 nm irradiation are equal.

For 8F-AZB, it is confirmed that irradiation at 532 nm induces a higher conversion to its *cis* isomer in the cuvette than in the microchannel. In contrast, the microchannel exhibits a greater conversion back to the *trans*-isomer compared to the cuvette. Although both photoswitches without prior treatment of the solutions can contain both isomers, 8F-AZB is particularly sensitive to ambient light promoting the conversion to the *cis*-isomer.[51] If the initial *cis* fraction is already elevated, as can be seen for the microchannel in Fig. 3(e), the additional increase in *cis* population upon 532 nm irradiation is consequently reduced, which explains the comparably low $R_{cis\%}$. Conversely, 450 nm light drives the *cis*-to-*trans* conversion of both the *cis* isomers generated during 532 nm illumination and those present in the initial state, leading to a significantly larger $R_{trans\%}$ for the microchannel. This behaviour is also observed for AZB, despite the lower photoconversion percentage which could be due to the not optimal 365 nm excitation wavelength.

Interestingly, the initial and final states of AZB display an almost complete matching after the photoinduced *cis–trans* isomerizations: this confirms that fluorinated azobenzenes exhibit altered switching characteristics compared to AZB, including incomplete spectral recovery under visible irradiation.[52]

Taken together, the above results show that the effect of light irradiation is more evident when the solution is contained in the microchannel than in the cuvette. This enhanced response arises from the significantly shorter path length inside the microfluidic device, which allows more uniform excitation throughout the sample. Therefore, the microfluidic device enables efficient photoexcitation using both UV and visible light, demonstrating effective light penetration and optical performance.

SAXS measurements

Due to their sub-nanometer molecular dimensions and inherently low scattering contrast relative to the solvent, AZB and 8F-AZB are not well suited to be analyzed by SAXS. Therefore, to demonstrate that the device can be used for X-ray techniques during laser-induced photoexcitation, Hb was selected as a model system because its CO-bound form (HbCO) is photosensitive and undergoes well-characterized structural changes upon photoactivation, which can be monitored by SAXS. Hb is a tetrameric protein composed of two identical dimers, and it exists in at least two different quaternary structures in solution: the relaxed (R) structure and a tense (T) state. The R structure is stabilized by adding ligands like CO, while the T state predominates when the protein is unligated. The R-to-T transition involves conformational changes both of tertiary and of quaternary structure.[53] A laser pulse in the green wavelength range can photolyze HbCO triggering the R-to-T transition.[12]

Initially, Hb was measured in a standard 1.5 mm diameter quartz capillary, commonly used for SAXS experiments, which served as a reference for subsequent measurements performed in the microchannel. Five 10 s exposures were acquired, and the corresponding scattering curves were averaged.

The SAXS pattern with the Guinier fit and the R_g value are shown in Fig. 4(a). After the capillary measurements, the empty microfluidic channel was positioned for SAXS experiments. Its alignment to the X-ray beam was achieved by translating the device along the z axis while monitoring the transmission signal with a photodiode positioned on the beamstop. The variation in transmission through the device (top lid, channel walls, bottom lid) allowed the precise identification of the channel center, as shown in Fig. 2(b). Because the top and bottom lids absorb X-rays more than the channel walls, the center of the channel is therefore the one in which the transmission is relatively higher. After alignment, Hb and HbCO were measured while slowly flowing in the channel at 0.25 μl min^{-1}. First, to assess radiation damage, 160 exposures of 10 s with 1 s delay were acquired for each protein. The first and last scattering curve were compared (Fig. S4 of SI) and no difference was observed. In addition, the invariant and the correlation length were calculated for each measurement (data not shown), presenting no variation and confirming the absence of radiation damage. Then, twenty 10 s exposures were collected both for Hb and for HbCO, and the average of the corresponding scattering curves with the Guinier fit are shown in Fig. 4(b). Finally, 40 exposures of 0.1 s were taken for HbCO and averaged (result shown in Fig. 4(c) together with the Guinier fit and R_g value).

A high protein concentration was intentionally used for both Hb and HbCO. High concentrations are usually employed for time-resolved pump–probe SAXS/WAXS studies of photosensitive proteins, as suggested by literature (*i.e.* 18–20 mg ml^{-1} for Sensory rhodopsin II,[54] 30 mg ml^{-1} for phytochromes,[55] 50 mg ml^{-1} for human cyclophilin A[56] and for PYP,[19] higher than 70 mg ml^{-1} for HbCO[12]). This is motivated by the need to resolve extremely subtle differences arising from the internal protein structure. Accordingly, the analysis focuses on differences in the scattering signal at higher q values, which are sensitive to internal structural features while being less affected by the aggregation effects that typically become relevant at such concentrations.

The internal volume of the device is small (10 μl), thus rendering such measurements efficient and economical, even with costly or limited protein samples. In principle, a dilution series could be performed for each protein to identify the optimal concentration for SAXS.

For the concentration tested here, aggregation was observed as indicated by the strong increase in scattering intensity at $q <$

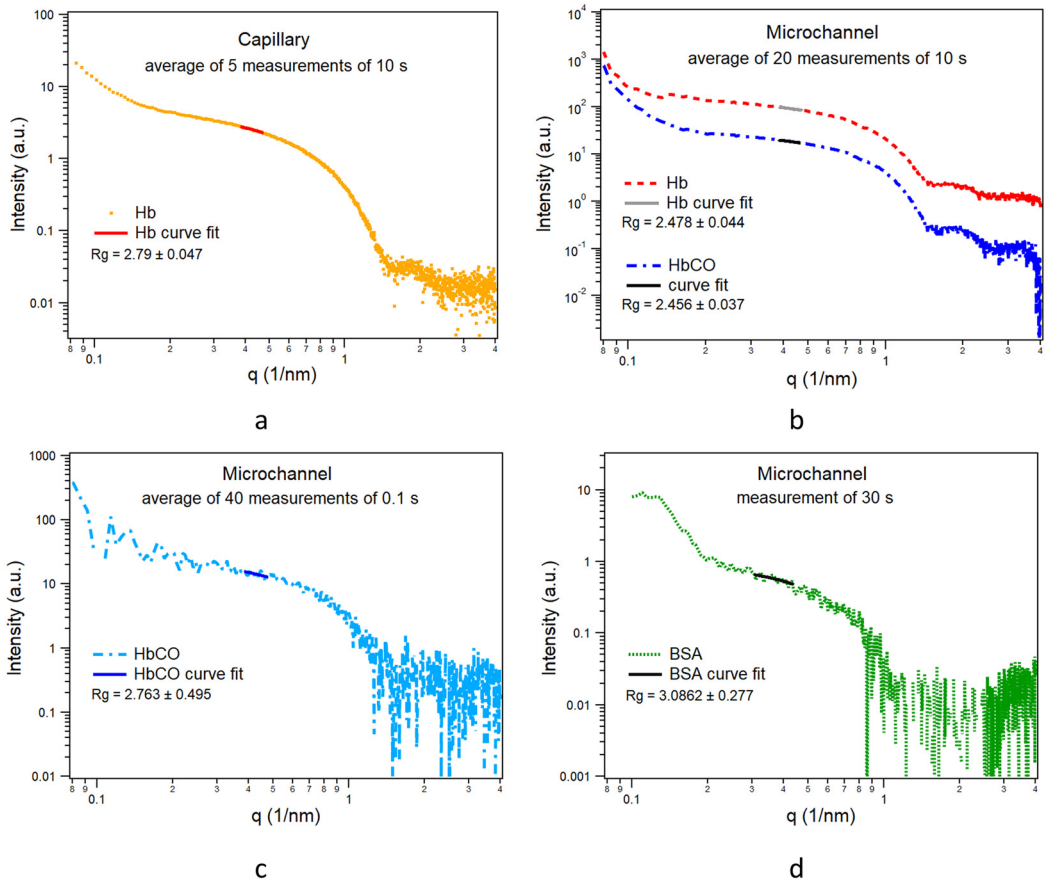

Fig. 4 Scattering curves with corresponding Guinier fit. The values of R_g are reported. (a) Hb in the capillary (yellow dotted line) and fit (red continuous line). The curve is obtained averaging five measurements of 10 s. (b) Hb (red dashed line) with corresponding fit (continuous grey line) and HbCO (blue dashed with dots line) with corresponding fit (continuous black line) in the microchannel. The scattering curves are obtained averaging 20 measurements of 10 s. The curves are shifted in vertical for clarity. (c) HbCO (light blue dashed with dots line) with corresponding fit (continuous blue line) in the microchannel. The scattering curve is an average of 40 measurements of 0.1 s. (d) BSA (green dashed line) with corresponding fit (continuous black line). The scattering curve was measured with a single exposure of 30 s.

0.2 nm^{-1} visible in the scattering curves displayed in Fig. 4. Nevertheless, this does not hinder comparison between the capillary and microchannel measurements. As shown in Fig. 4(a) and (b), the SAXS measurement of Hb in the microchannel is comparable to that collected in the standard capillary, demonstrating that the microfluidic device can be used to perform SAXS experiments under conditions equivalent to conventional setups. For both Hb and HbCO, determination of $p(r)$ and fits of the indirect Fourier transform were obtained using the GNOM program,[45] highlighting the ability of the device to distinguish subtle conformational changes in proteins (Fig. S5 of SI).

By averaging a sufficient number of frames, the resulting scattering curves present a good signal-to-noise even in the higher q range (q = 1–4 nm^{-1}), allowing the detection of the difference between Hb and HbCO (Fig. 4(b)), which arise from the tertiary and quaternary structural changes.[12]

All Hb and HbCO curves were fitted in the same q range as for the capillary SAXS data to determine the radius of gyration R_g, where the lower q value was selected to minimize the effect of aggregation. The resulting R_g values shown in Fig. 4(b) and (c) were found consistent across all measurements within the experimental error, and in agreement with previously reported literature values (2.567 nm for Hb and 2.465 nm for HbCO),[57] demonstrating that the fabricated microchannel allows SAXS measurements with short acquisition times while maintaining a good signal-to-noise ratio.

To show that smaller concentration of proteins can still be detected, a solution of 5 mg ml^{-1} of bovine serum albumin (BSA) in 50 mM HEPES buffer at pH 7.5 was measured for 30 s in the microchannel. The scattering curve, together with the fit of the Guinier approximation, is presented in Fig. 4(d). The R_g value is consistent with the one reported in literature (2.99 nm).[58]

To evaluate the device performance under photoexcitation conditions (513 nm), SAXS measurements for HbCO were first acquired for 10 s without illumination (laser OFF), followed by measurements of 10 s under continuous irradiation (laser ON). The scattering curves were compared. Three laser powers were employed to evaluate the effect of photodamage of the protein sample. For laser powers of 2.6 mW and 62 mW, the difference curves (ON minus OFF) oscillate around zero (Fig. S6), which

indicates no photodamage. In contrast, at 182 mW, significant sample damage occurred without flowing the protein (Fig. S7(a)) as well as when flowing it at 100 μL min^{-1}, which corresponds to a residence time of about 0.5 s under irradiation (Fig. S7(b)).

Protein damage typically leads to adhesion to the container walls, whether in capillaries or in microchannels. Hence, the microchannel was routinely cleaned after every protein measurement by flushing with Milli-Q water. The successful cleaning after the 160 frames radiation damage test on Hb and HbCO is demonstrated in Fig. S8(a). In the case of pronounced protein damage, like after laser irradiation at P = 182 mW, rinsing with water alone was not sufficient to remove residual protein from the channel. Therefore, a 1% v/v aqueous solution of Hellmanex III was employed, followed by thorough flushing with Milli-Q water. Owing to the chemical resistance of SUEX, the device could be efficiently cleaned and reused, as confirmed by the identical buffer scattering curves, recorded before and after treatment with Hellmanex III, in Fig. S8(b).

In the next step, experiments were conducted by continuously acquiring SAXS images with 0.1 s exposure time initially with the light source OFF, and then switching it ON to monitor the resulting changes. Again, the three laser power values used previously were tested (P = 2.6 mW, 62 mW and 182 mW), with HbCO and buffer measured under a flow rate of 100 μl min^{-1}. For completeness, the empty microchannel was also measured. From each dataset, Q and the l_c were determined as a function of time (Fig. 5 and S9 of SI). At 2.6 mW and 62 mW, l_c remained constant for protein, buffer and empty device, whereas at 182 mW, changes were observed only for the protein. As l_c reflects the characteristic dimensions of the protein, these results confirm the absence of laser damage at illumination powers of P = 2.6 and 62 mW, while at P = 182 mW pronounced photodamage occurs, leading to protein degradation.

When considering Q, no changes are observed at 2.6 mW, whilst at 62 mW and 182 mW, illumination produced a pronounced signal jump, that increased with laser power. This effect was observed for the protein, the buffer, and the empty channel. This behaviour is attributed to a laser-induced thermocapillary effect,[27] where energy from the laser heats the microchannel and the sample, resulting in a scattering signal which is convoluted with the scattering signature of the protein structural changes. A similar effect was reported by Cammarata *et al.*,[12] who suggested decoupling heating and photolysis contributions by subtracting the signal taken after photolysis recovery but before thermal relaxation (for HbCO, this occurs within 32 ms). It can also be noted that the magnitude of the thermal jump increases with laser power.

The microchannel could, in principle, be used for temperature-jump (T-jump) experiments. In such applications, the contribution of the channel itself must be considered, and the T-jump can be calibrated by measuring samples with known structural transitions at defined temperatures. This approach has been previously demonstrated by our group using a phospholipid for slow temperature changes,[59] and by Prassl *et al.* using lipoproteins for fast variations.[60]

In the present work, the primary focus was on the development and validation of the microfluidic device, specifically assessing whether the optimized optical path length enables homogeneous photoexcitation of the entire sample volume, in contrast to conventional SAXS capillaries with larger path lengths. Here, the experiments were intentionally conducted on timescales substantially longer than those associated with photo-induced internal structural rearrangements of HbCO. Consequently, the measurements are not sensitive to transient structural intermediates but rather serve to validate the experimental approach and device performance, with

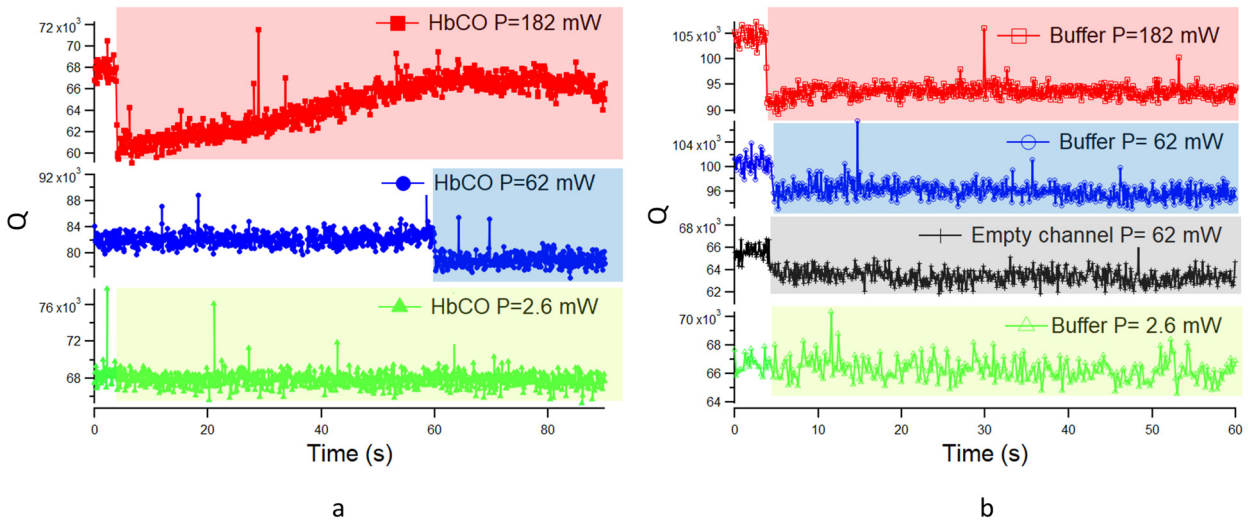

Fig. 5 (a) Calculated invariant *vs.* SAXS exposure time for the protein inside the microfluidic device flowing at 100 μl min^{-1}. During the SAXS measurement the laser is turned ON. The shadowed area corresponds to the measurements done with laser ON. Different laser power values are shown. The laser with P = 62 mW was turned ON around one minute after starting the measurement. (b) Calculated invariant *vs.* SAXS exposure time for the buffer inside the microfluidic device flowing at 100 μl min^{-1} and for the empty channel.

photodamage representing the dominant observable effect under strong laser power conditions (P = 182 mW). Resolving the associated structural transition would therefore require a pump–probe experimental scheme. Under such conditions, the inherently low signal-to-noise ratio becomes a critical limitation. To optimize the detection of time-dependent scattering differences between the photoexcited and ground states, several strategies are essential, including the use of a high-brilliance beamline, the selection of an appropriate q-range sensitive to the relevant structural changes, and, most importantly, the optimization of the acquisition protocol through increased repetition (10^6) and extensive signal averaging. In the case of the present research conducted at the Austrian SAXS beamline@Elettra, for 1 s of exposure time in normal operation, around 12 minutes would be needed in a single pulse pump–probe configuration with standard hybrid filling.

These preliminary SAXS experiments demonstrate that the described microfluidic device could be used for photoexcitation or T-jump studies on proteins, as well as on other photosensitive samples, highlighting its versatility and potential for a wide range of time-resolved structural investigations.

Conclusions

In this work, a microfluidic device is developed that allows illumination of the sample with visible and UV light down to 280 nm in one direction, and is transparent to X-rays in the perpendicular direction. Fabricated using standard UV lithography combined with SUEX dry resist lamination on IM-PMMA, the device does not necessarily require a cleanroom and can be downscaled to tens of microns, limited only by the dry film resist resolution. The device was successfully employed for photoexcitation experiments monitored by either UV-vis spectroscopy in the visible range or by SAXS. Its small channel dimensions ensure full excitation of the sample across the investigated wavelengths (365 nm, 450 nm, 513 nm, 532 nm). SAXS measurements of proteins in the microchannel demonstrate that subtle structural differences, such as between Hb and HbCO, can be detected while fully exploiting the low sample consumption allowed by microfluidics. Generally, the presented research provides an approach to fabricate microfluidic devices whose dimensions can be independently tailored to match both the absorption length of the illumination light in one direction, and the size and penetration depth of the X-ray beam on the perpendicular one, thus optimizing the photoexcitation conditions for SAXS experiments. The device is easily cleaned and reused, as its materials are compatible with standard protein and lipid cleaning solutions. This versatile platform would enable photoexcitation studies and laser-induced thermal jump (T-jump) experiments. While its performance has been optimized and demonstrated on photosensitive proteins, it can be readily applied to inorganic or hybrid systems, or in experiments that require simultaneous optical excitation and X-ray probing (pump–probe configurations). More complex device geometries are also possible, including mixing regions before the observation channel. Moreover, the device could be operated in a 'light-reconfigurable' way[27] where injection, pumping, mixing, and sorting are controlled by light in one direction, while structural characterization is simultaneously performed with X-rays in the perpendicular direction. By combining microfluidics with simultaneous optical and X-ray transparency, this platform overcomes limitations of illumination efficiency, detection of subtle structural changes and temporal control, enabling new opportunities for time-resolved structural studies across biology, chemistry, and materials science.

Author contributions

B. M. conceptualization, investigation, device fabrication, formal analysis, draft writing. S. K. conceptualization, investigation, formal analysis. B. S. investigation, formal analysis. A. T. and M. R. device fabrication. H. A. conceptualization, SAXS investigation, formal analysis, fund raising. All authors contributed to review and editing of the manuscript.

Conflicts of interest

There are no conflicts to declare.

Data availability

Data generated for this article, including UV-vis and SAXS experiments, are accessible at the TU Graz Repository https://doi.org/10.3217/bvydb-4ak58.

Supplementary information (SI) is available. See DOI: https://doi.org/10.1039/d5lc01116g.

Acknowledgements

The authors gratefully thank Ing. A. Radeticchio and C. Morello for technical assistance, and Ass. Prof. H. A. Reichl and M. Rödl for providing the fluoro-azobenzene compounds. The authors further acknowledge Y. Roque-Diaz and Dr. G. Milcovich for some helpful assistance to experiment (CERIC-ERIC proposal no. 20237222). This work was published with the support of TU Graz Open Access Publishing Fund.

Notes and references

1 W. A. Velema, J. P. Van Der Berg, M. J. Hansen, W. Szymanski, A. J. M. Driessen and B. L. Feringa, *Nat. Chem.*, 2013, **5**, 924–928.
2 Z. Chu, C. A. Dreiss and Y. Feng, *Chem. Soc. Rev.*, 2013, **42**, 7174–7203.
3 G. Mayer and A. Hechel, *Angew. Chem., Int. Ed.*, 2006, **45**, 4900–4921.
4 J. Andersson, S. Li, P. Lincoln and J. Andréasson, *J. Am. Chem. Soc.*, 2008, **130**, 11836–11837.
5 M. Borowiak, W. Nahaboo, M. Reynders, K. Nekolla, P. Jalinot, J. Hasserodt, M. Rehberg, M. Delattre, S. Zahler, A. Vollmar, D. Trauner and O. Thorn-Seshold, *Cell*, 2015, **162**, 403–411.

6 I. Tochitsky, M. R. Banghart, A. Mourot, J. Z. Yao, B. Gaub, R. H. Kramer and D. Trauner, *Nat. Chem.*, 2012, **4**, 105–111.
7 H. Rau, in *Photoreactive Organic thin films*, ed. Z. Sekkat and W. Knoll, Academic Press, San Diego, California (USA), 1st edn, 2002, vol. 1(1), pp. 3–47.
8 Z. Li, H. Wang, M. Chu, P. Guan, Y. Zhao, Y. Zhao and J. Wang, *RSC Adv.*, 2017, **7**, 44688–44695.
9 J. Eastoe and A. Vesperinas, *Soft Matter*, 2005, **1**, 338–347.
10 S. D. Pritzl, J. Morstein, N. A. Pritzl, J. Lipfert, T. Lohmüller and D. H. Trauner, *Commun. Mater.*, 2025, **6**, 59.
11 R. S. H. Liu and L. U. Colmenares, *Proc. Natl. Acad. Sci. U. S. A.*, 2003, **25**, 14639–14644.
12 M. Cammarata, M. Levantino, F. Schotte, P. A. Anfinrud, F. Ewald, J. Choi, A. Cupane, M. Wulff and H. Ihee, *Nat. Methods*, 2008, **5**, 881–886.
13 J. Woodhouse, G. Nass Kovacs, N. Coquelle, L. M. Uriarte, V. Adam, T. R. M. Barends, M. Byrdin, E. de la Mora, R. Bruce Doak, M. Feliks, M. Field, F. Fieschi, V. Guillon, S. Jakobs, Y. Joti, P. Macheboeuf, K. Motomura, K. Nass, S. Owada, C. M. Roome, C. Ruckebusch, G. Schirò, R. L. Shoeman, M. Thepaut, T. Togashi, K. Tono, M. Yabashi, M. Cammarata, L. Foucar, D. Bourgeois, M. Sliwa, J. P. Colletier, I. Schlichting and M. Weik, *Nat. Commun.*, 2020, **11**, 741.
14 C. Weber, L. Pithan, A. Zykov, S. Bommel, F. Carla, R. Felici, C. Knie, D. Bléger and S. Kowarik, *J. Phys.: Condens. Matter*, 2017, **29**, 434001.
15 H. Poddar, D. J. Heyes, G. Schirò, M. Weik, D. Leys and N. S. Scrutton, *FEBS J.*, 2022, **289**, 576–595.
16 J. Royes, V. A. Bjørnestad, G. Brun, T. Narayanan, R. Lund and C. Tribet, *J. Colloid Interface Sci.*, 2022, **610**, 830–841.
17 M. F. Ober, A. Müller-Deku, A. Baptist, B. Ajanović, H. Amenitsch, O. Thorn-Seshold and B. Nickel, *Nanophotonics*, 2022, **11**, 2361–2368.
18 F. Schotte, H. S. Cho, F. Dyda and P. Anfinrud, *Struct. Dyn.*, 2024, **11**, 021303.
19 H. S. Cho, F. Schotte, N. Dashdorj, J. Kyndt, R. Henning and P. A. Anfinrud, *J. Am. Chem. Soc.*, 2016, **138**, 8815–8823.
20 M. Levantino, G. Schirò, H. T. Lemke, G. Cottone, J. M. Glownia, D. Zhu, M. Chollet, H. Ihee, A. Cupane and M. Cammarata, *Nat. Commun.*, 2015, **6**, 7772.
21 L. Buglioni, F. Raymenants, A. Slattery, S. D. A. Zondag and T. Noël, *Chem. Rev.*, 2022, **122**, 2752–2906.
22 G. M. Whitesides, *Nature*, 2006, **44**, 368–373.
23 Y. Liu and X. Jiang, *Lab Chip*, 2017, **17**, 3960–3978.
24 A. Ghazal, J. P. Lafleur, K. Mortensen, J. P. Kutter, L. Arleth and G. V. Jensen, *Lab Chip*, 2016, **16**, 4263–4295.
25 B. F. B. Silva, *Phys. Chem. Chem. Phys.*, 2017, **19**, 23690–23703.
26 M. A. Levenstein, C. Chevallard, F. Malloggi, F. Testard and O. Taché, *Lab Chip*, 2025, **25**, 1169–1227.
27 D. Baigl, *Lab Chip*, 2012, **12**, 3637–3653.
28 T. Kurdadze, F. Lamadie, K. A. Nehme, S. Teychené, B. Biscans and I. Rodriguez-Ruiz, *Sensors*, 2024, **24**, 1529.
29 D. Cojoc, H. Amenitsch, E. Ferrari, S. C. Santucci, B. Sartori, M. Rappolt, B. Marmiroli, M. Burghammer and C. Riekel, *Appl. Phys. Lett.*, 2010, **97**, 244101.
30 S. C. Santucci, D. Cojoc, H. Amenitsch, B. Marmiroli, B. Sartori, M. Burghammer, S. Schoeder, E. Dicola, M. Reynolds and C. Riekel, *Anal. Chem.*, 2011, **83**(12), 4863–4870.
31 E. Vergucht, T. Brans, F. Beunis, J. Garrevoet, S. Bauters, M. De Rijcke, D. Deruytter, C. Janssen, C. Riekel, M. Burghammer and L. Vincze, *J. Synchrotron Radiat.*, 2015, **22**, 1096–1105.
32 L. C. McKenzie, P. M. Haben, S. D. Kevan and J. E. Hutchison, *J. Phys. Chem. C*, 2010, **114**, 22055–22063.
33 M. Herbst, E. Hofmann and S. Förster, *Langmuir*, 2019, **35**, 11702–11709.
34 O. McCubbin Stepanic, C. J. Pollock, K. A. Zielinski, W. Foschi, D. B. Rice, L. Pollack and S. DeBeer, *Rev. Sci. Instrum.*, 2025, **96**, 015107.
35 R. K. Ramamoorthy, E. Yildirim, I. Rodriguez-Ruiz, P. Roblin, L. M. Lacroix, A. Diaz, R. Parmar, S. Teychené and G. Viau, *Lab Chip*, 2023, **24**, 327–338.
36 Y. Cao, J. Floehr, S. Ingebrandt and U. Schnakenberg, *Micromachines*, 2021, **12**, 632.
37 A. El Hasni, S. Pfirrmann, A. Kolander, E. Yacoub-George, M. König, C. Landesberger, A. Voigt, G. Grützner and U. Schnakenberg, *Microfluid. Nanofluid.*, 2017, **21**, 41.
38 M. M. Roos, A. Winkler, M. Nilsen, S. B. Menzel and S. Strehle, *Int. J. Precis. Eng. Manuf.-Green Technol.*, 2022, **9**, 43–57.
39 M. Rödl, K. Küssner and H. A. Schwartz, *Z. Anorg. Allg. Chem.*, 2024, **650**, e202400018.
40 Z. Wang, Q. Jiang, C. Barwig, A. Mishra, K. Ramesh and C. Selhuber-Unkel, *JPhys Photonics*, 2024, **6**, 035024.
41 H. Amenitsch, M. Rappolt, M. Kriechbaum, H. Mio, P. Laggner and S. Bernstorff, *J. Synchrotron Radiat.*, 1998, **5**, 506–508.
42 M. Burian, C. Meisenbichler, D. Naumenko and H. Amenitsch, *J. Appl. Crystallogr.*, 2022, **55**, 677–685.
43 O. Glatter, in *Scattering Methods and their Application in Colloid and Interface Science*, Elsevier, 2018.
44 J. Trewhella, A. P. Duff, D. Durand, F. Gabel, J. M. Guss, W. A. Hendrickson, G. L. Hura, D. A. Jacques, N. M. Kirby, A. H. Kwan, J. Pérez, L. Pollack, T. M. Ryan, A. Sali, D. Schneidman-Duhovny, T. Schwede, D. I. Svergun, M. Sugiyama, J. A. Tainer, P. Vachette, J. Westbrook and A. E. Whitten, *Acta Crystallogr., Sect. D:Struct. Biol.*, 2017, **73**, 710–728.
45 D. I. Svergun, *J. Appl. Crystallogr.*, 1992, **25**, 495–503.
46 M. Burian, B. Marmiroli, A. Radeticchio, C. Morello, D. Naumenko, G. Biasiol and H. Amenitsch, *J. Synchrotron Radiat.*, 2020, **27**, 51–59.
47 H. S. Cho, F. Schotte, V. Stadnytskyi, A. Dichiara, R. Henning and P. Anfinrud, *J. Phys. Chem. B*, 2018, **122**, 11488–11496.
48 R. Haider, B. Marmiroli, I. Gavalas, M. Wolf, M. Matteucci, R. Taboryski, A. Boisen, E. Stratakis and H. Amenitsch, *Microelectron. Eng.*, 2018, **195**, 7–12.
49 D. Orthaber, A. Bergmann and O. Glatter, *J. Appl. Crystallogr.*, 1999, **33**, 218–225.
50 C. Knie, M. Utecht, F. Zhao, H. Kulla, S. Kovalenko, A. M. Brouwer, P. Saalfrank, S. Hecht and D. Bléger, *Chem. – Eur. J.*, 2014, **20**, 16492–16501.

51 S. L. Barret, C. Meyer, E. Cwiklik, V. Fieglein, M. Burns, J. Guerrero and W. J. Brittain, *J. Photochem. Photobiol., A*, 2024, **446**, 115114.
52 M. Rödl, A. Reka, M. Panic, A. Fischereder, M. Oberlechner, T. Mairegger, H. Kopacka, H. Huppertz, T. S. Hofer and H. A. Schwartz, *Langmuir*, 2022, **38**, 4295–4309.
53 W. A. Eaton, E. R. Henry, J. Hofrichter, S. Bettati, C. Viappiani and A. Mozzarelli, *IUBMB Life*, 2007, **59**(8–9), 586–599.
54 L. Ostojić, D. Sarabi, R. Bosman, G. Ortolani, S. Ghosh, M. N. Pedersen, M. Sander, P. Båth, G. Hammarin, R. Dods, P. Norder, C. Safari, M. Wulff, M. Levantino, G. Brändén and R. Neutze, *Structure*, 2026, **34**, 1–12.
55 H. Takala, S. Niebling, O. Berntsson, A. Björling, H. Lehtivuori, H. Häkkänen, M. Panman, E. Gustavsson, M. Hoernke, G. Newby, F. Zontone, M. Wulff, A. Menzel, J. A. Ihalainen and S. Westenhoff, *Struct. Dyn.*, 2016, **3**, 054701.
56 M. C. Thompson, B. A. Barad, A. M. Wolff, H. Sun Cho, F. Schotte, D. M. C. Schwarz, P. Anfinrud and J. S. Fraser, *Nat. Chem.*, 2019, **11**, 1058–1066.
57 J. Lal, M. Maccarini, P. Fouquet, N. T. Ho, C. Ho and L. Makowski, *Protein Sci.*, 2017, **26**, 505–514.
58 E. Mylonas and D. I. Svergun, *J. Appl. Crystallogr.*, 2007, **40**, s245–s249.
59 R. Haider, B. Sartori, A. Radeticchio, M. Wolf, S. D. Zilio, B. Marmiroli and H. Amenitsch, *J. Appl. Crystallogr.*, 2021, **54**, 132–141.
60 R. Prassl, M. Pregetter, H. Amenitsch, M. Kriechbaum, R. Schwarzenbacher, J. M. Chapman and P. Laggner, *PLoS One*, 2008, **3**(12), e4079.

